SUPPLEMENTARY INFORMATION

Berry paramagnetism in Dirac semimetal $ZrTe_5$

Sanghyun Ji[1], Sang-Eon Lee[1], Myung-Hwa Jung[1*]

[1]Department of Physics, Sogang University, Seoul 04107, Korea

Supplementary Note 1: Comparison between previous work and the present work

Supplementary Note 2: Two carrier model fitting

Supplementary Note 3: Magnetization for all crystal axes and samples

Supplementary Note 4: Evaluation of band parameters of $ZrTe_5$

Supplementary Note 5: Comparison between quantum lifetime and transport lifetime

Supplementary Note 6: The model for calculation of a magnetization

Supplementary Note 7: Crystal axis-dependent Berry paramagnetism

Supplementary Note 8: Diamagnetism-dominant magnetization

Supplementary Note 1: Comparison between previous work and the present work

Supplementary Figure 1 shows temperature-dependent resistivities and magnetizations of $ZrTe_5$ of previous and present works. Although a similar analytical method was used to $ZrTe_5$ in Ref. 1, we would emphasize the significant difference between their and our samples. The most distinguished points are shown in Supplementary Figure 1. $ZrTe_5$ used in Ref. 1 displays the resistivity peak at T_p = 34 K, interpreted as a topological phase transition, while $ZrTe_5$ in our study exhibits the typical behavior of Lifshitz transition at T_p = 122 K. Note that the magnetization shown in Ref. 1 monotonically decreases with increasing temperature compared to our result showing the magnetic susceptibility minimum at T_m (= T_p). Importantly, in our study, we demonstrate the correlation between electrical resistivity and magnetic susceptibility. The susceptibility in our work shows negative responses regardless of the magnetic field strength. This result is different from that of Ref. 1, showing the positive low-field magnetic response. This result can be explained by different topological band structures: They have two Dirac bands, while we have a single Dirac band with a trivial band.

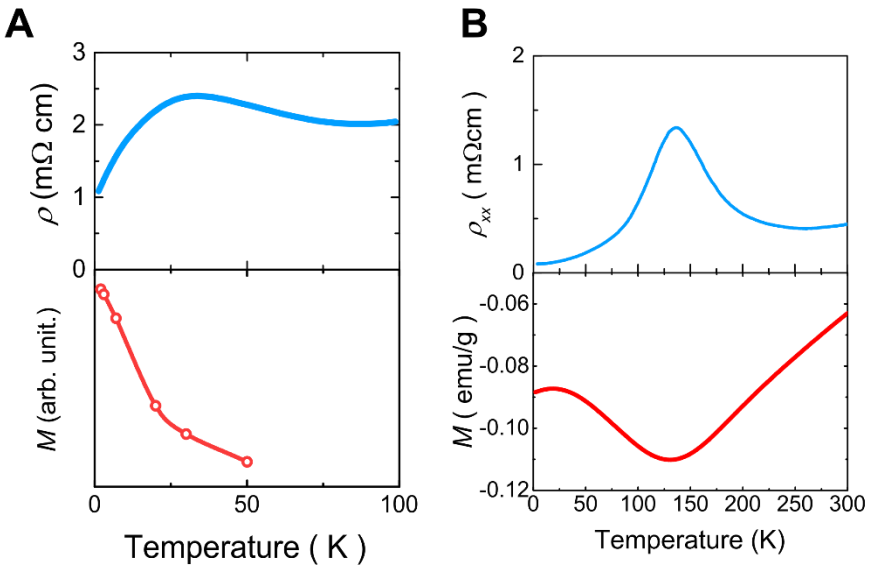

Supplementary Figure 1. Temperature-dependent resistivity and magnetization, $\rho(T)$ and $M(T)$, for $ZrTe_5$ taken from (A) Ref. 1 and (B) this study.

Supplementary Note 2: Two-carrier model fitting

The two-carrier model was adopted to evaluate values of carrier density and mobility. The measured magnetoresistivity and the hall resistivity were translated into conductivity, $\sigma_{xx} = \frac{\rho_{xx}}{\rho_{xx}^2+\rho_{xy}^2}, \sigma_{xy} = \frac{\rho_{xy}}{\rho_{xx}^2+\rho_{xy}^2}$, as shown in Supplementary Figure 2. Furthermore, the σ_{xx} and σ_{xy} were simultaneously fitted by the two carrier model, $\sigma_{xx} = \frac{n_1 q\mu_1}{1+(\mu_1 B)^2} + \frac{\sigma_{xx}(0)-n_1 q\mu_1}{1+(\mu_2 B)^2}$ and $\sigma_{xy} = \left[n_1\mu_1^2 \frac{1}{1+(\mu_1 B)^2} + n_2\mu_2^2 \frac{1}{1+(\mu_2 B)^2}\right] eB$ with global parameters n_1, n_2, μ_1, μ_2, where μ_i represents the mobility of carrier i and n_i denotes the carrier density of carrier i. The carrier density, n_i, has a negative value when the carrier is the electron and a positive value for the hole.

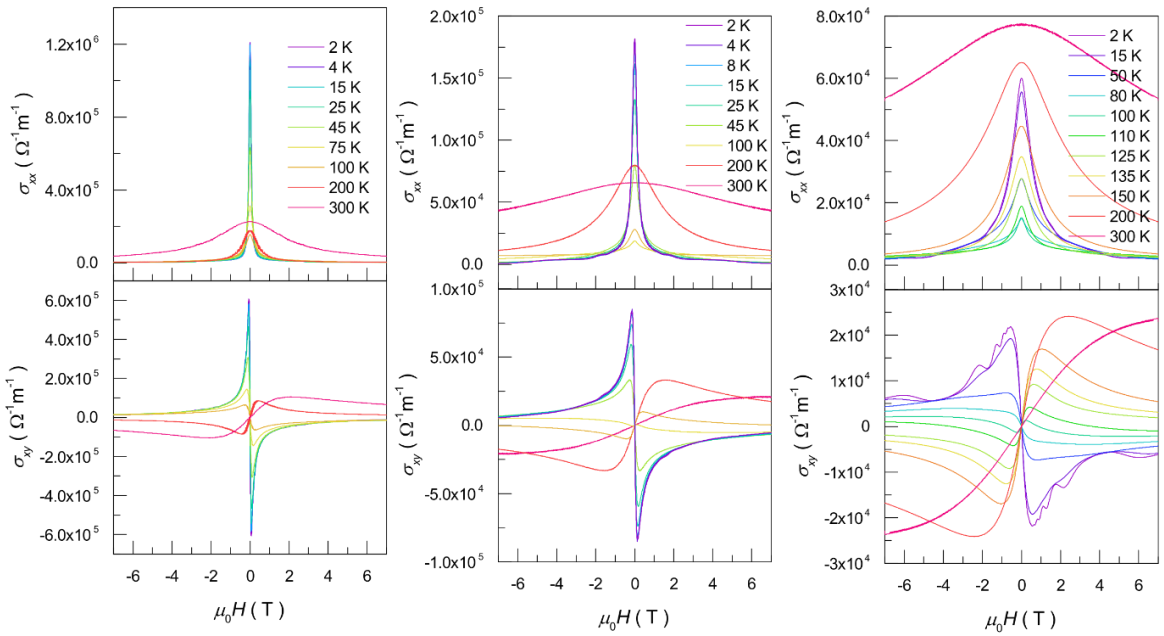

Supplementary Figure 2. σ_{xx} and σ_{xy} curves of x = 0, 0.1, and 0.2, respectively.

Supplementary Note 3: Magnetization for all crystal axes and samples

Supplementary Figure 3 shows the magnetization curves for x = 0, 0.1 and 0.2. Evidently, a diamagnetic contribution and quantum oscillations are prominent when the magnetic field is applied along the b axis.

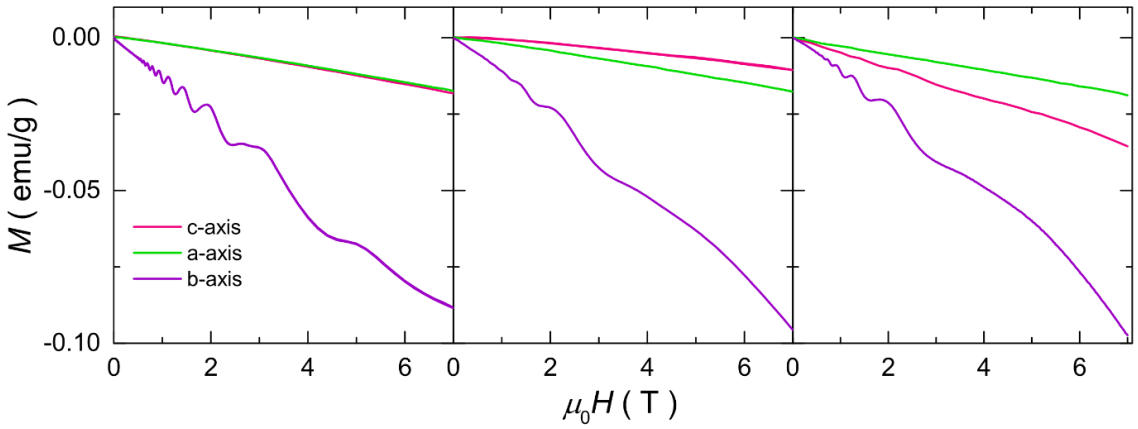

Supplementary Figure 3. The magnetization curves for all the crystal axes for x = 0, 0.1 and 0.2, respectively.

Supplementary Note 4: Evaluation of band parameters of $ZrTe_5$

We evaluate band parameters of $ZrTe_5$ from the quantity measured in the Hall effect and quantum oscillations. The cyclotron mass is $m_c = \frac{\hbar^2}{2\pi}\frac{\partial A}{\partial E}$, where the Fermi surface cross-section A is $A = \pi k_x^F k_y^F$ when the magnetic field is along the *z* axis. Then, $\frac{\hbar^2}{2\pi}\frac{\partial A}{\partial E} = \frac{\hbar^2}{2\pi}(\frac{(\partial A)}{\partial k_x}\left(\frac{\partial E}{\partial k_x}\right)^{-1} + \frac{(\partial A)}{\partial k_y}\left(\frac{\partial E}{\partial k_y}\right)^{-1})$. Assuming gapless linear dispersion, $E = \hbar k \cdot v$, it becomes $\frac{\hbar^2}{2\pi}\frac{\partial A}{\partial E} = \frac{\hbar}{2v_x v_y}(v_x k_x^F + v_y k_y^F) = \frac{E^F}{v_x v_y}$. Assuming that the Fermi surface is smooth ellipsoid and $v_y = \eta v_x$, then $m_c = \frac{\hbar}{2\eta v_x}\left(k_x^F + \eta k_y^F\right) \propto \frac{\hbar k_x^F}{v_x}$. We evaluated Fermi momentums, $k_a^F = 8.55 \times 10^7\ m^{-1}, k_b^F = 8.41 \times 10^8\ m^{-1}\ and\ k_c^F = 1.77 \times 10^8\ m^{-1}$, with the carrier density of $n = \frac{2}{(2\pi)^3}\pi k_a^F k_b^F k_c^F$ and the quantum oscillation frequencies of $F_{ac}\ and\ F_{bc}$, where $F_{ij} = \frac{\hbar}{2\pi e}\pi k_i^F k_j^F$. From the relation, $E^F = \hbar v_a k_a^F = \hbar v_b k_b^F = \hbar v_c k_c^F$, we obtain the ratio, $\frac{v_i}{v_j} = \frac{k_j^F}{k_i^F}$ and the Fermi energy, $E^F \approx 30\ meV$. The results are shown in Supplementary Table. 1.

v_a (m/s)	v_b (m/s)	v_c (m/s)
5.39×10^5	5.48×10^4	2.60×10^5
k_a^F (m^{-1})	k_b^F (m^{-1})	k_c^F (m^{-1})
8.55×10^7	8.41×10^8	1.77×10^8
m^*_{bc}/m_e	m^*_{ac}/m_e	m^*_{ab}/m_e
0.37	0.038	0.18

Supplementary Table 1. Evaluated band parameters of $ZrTe_5$

Supplementary Note 5: Comparison between quantum lifetime and transport lifetime

We fitted the dHv oscillations to the Lifshitz-Kosevich formula using the effective mass from the temperature reduction factor fitting to obtain information of a lifetime. The solid red lines in Supplementary Figure 4 denote the fitted curves. The obtained quantum lifetime, τ_q, was 0.13 ps for x = 0, 0.048 ps for x = 0.1, and 0.086 ps for x = 0.2 sample. However, the other evaluated band parameter shows a systematic tendency. Further analysis may support this interpretation. The ratio of transport lifetime to quantum lifetime, $r = \tau_{tr}/\tau_q$, is often interpreted as the experimental proof of the backscattering suppression[2,3]. We evaluated the transport lifetime τ_{tr} by fitting the conductivities to the two-carrier model. As discussed, carrier 1 with higher mobility was expected to be a Dirac fermion and responsible for the dHv oscillation. The obtained lifetime of carrier 1 was much higher than the quantum lifetime. The ratio remained approximately the same and large up to x = 0.1, while a significant drop was observed for x = 0.2, as shown in Supplementary Table 2. Since the ratio corresponds to the backscattering suppression, we expect that the substitution ratio for x = 0.2 is quite large so that the backscattering by Ti impurity becomes pronounced.

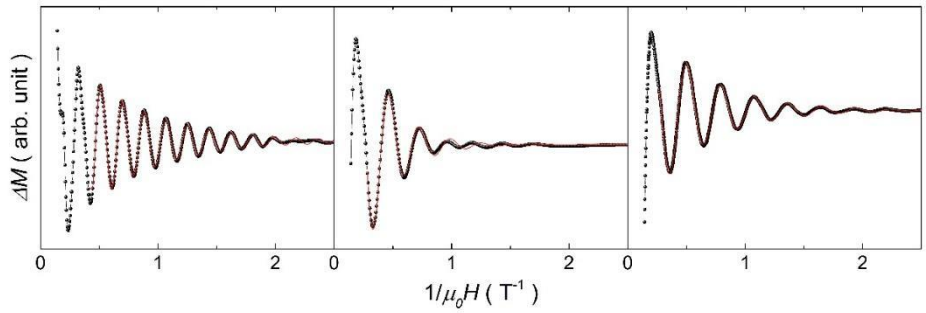

Supplementary Figure 4. Dingle factor fitting. The black lines denote experimental data, and the solid red lines represent the fitted curve of x=0, 0.1, and 0.2, respectively.

	x=0	x=0.1	x=0.2
τ_q	0.13 ps	0.048 ps	0.086 ps
τ_{tr}	3.7 ps	1.3 ps	0.31 ps
r	28	27	3.6

Supplementary Table 2. Evaluated transport lifetime, quantum lifetime, and lifetime ratio

Supplementary Note 6: The model to calculate the magnetization

We considered the same approach as already reported results[4,5] to simulate a magnetization of $ZrTe_5$. The quantum oscillatory signals were included. The Landau level for the calculation is $\varepsilon_{n,k,\pm} = \sqrt{(\hbar v_b k_b)^2 + 2e\hbar B n v_a v_c} \mp \frac{g\mu_B B}{2}$ $for\ n \neq 0$ and $\varepsilon_{0,k} = \sqrt{(\hbar v_b k_b)^2 + \left(\frac{g\mu_B B}{2}\right)^2}$. The integration of $E = \frac{BA}{2\pi}\sum_{n=0}^{N}\int_0^{k_{cutoff}} \frac{dk}{2\pi}(2-\delta_{n,0})\varepsilon_{n,k} n_F(\varepsilon_{n,k}-\mu)$ was performed, where n denotes Landau level index, k represents the momentum along the magnetic field, μ is the chemic potential, and $n_F(\varepsilon_{n,k}-\mu)$ denotes the Fermi function. We chose the area, A, as the unity. The magnetization al was obtained by $M = -\frac{\partial E}{\partial B}$. We imposed the constraint of a constant number of particles by letting the chemical potential, μ, make the number integration at magnetic field $N(B) = \frac{BA}{2\pi}\sum_{n=0}^{N}\int_0^{k_{cutoff}} \frac{dk}{2\pi}(2-\delta_{n,0}) n_F(\varepsilon_{n,k}-\mu)$ equal to $N(B = 0.1\,T)$. We selected the range of the magnetic field as $0.5\,T \leq B \leq 8\,T$ for calculation because the calculation cost rapidly increases when the lower field value is used. The calculated chemical potential shown in Supplementary Figure 5 reproduces the previous result well[4]. Additionally, the various g-factors were used to simulate the experimental data; we found that the simulation provided the best result when the g-factor was set to 10. Additionally, the finite lifetime due to scattering can blur each Landau sublevel. Hence, the exponential factor associated with the Dingle factor of the Lifshitz-Kosevich formula was multiplied by the conduction band contribution before adding diamagnetic valence band contribution.

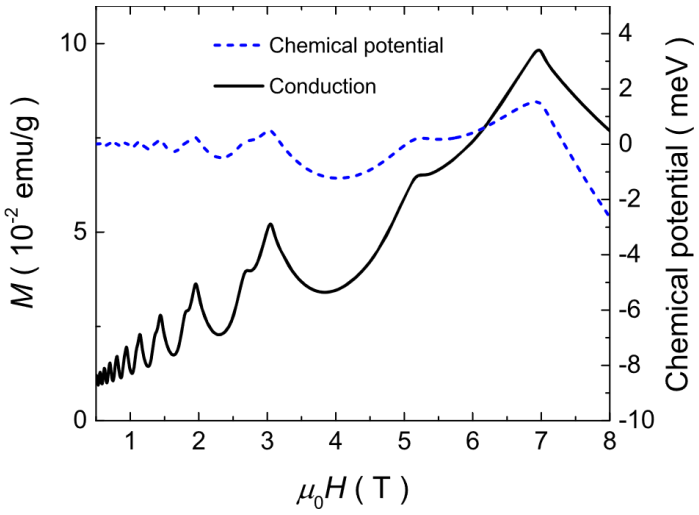

Supplementary Figure 5. Representative result of numerical calculation for the Berry paramagnetism of conduction band electrons. The Fermi energy is set to 31.85 meV (x = 0).

Supplementary Note 7: Crystal axis-dependent Berry paramagnetism

We simulated magnetizations when the magnetic field is applied along each crystal axis. Only the Berry paramagnetic contributions with quantum oscillations are plotted for clear comparison. Supplementary Figure 6 shows that the Berry paramagnetism is the largest when $H//b$ and highly suppressed when $H//a$ and $H//c$. The Landau levels are given as $\varepsilon_{n,k_i} = \sqrt{(\hbar v_i k_i)^2 + 2e\hbar B n v_j v_k}$ when the magnetic field direction is parallel to k_i. Since $v_b \ll v_a, v_c$, the density of state of 0th Landau level and the Landau level spacing is the largest when the field is applied along the *b* direction. Therefore, the Berry paramagnetism and quantum oscillations are most remarkable in the *b* direction.

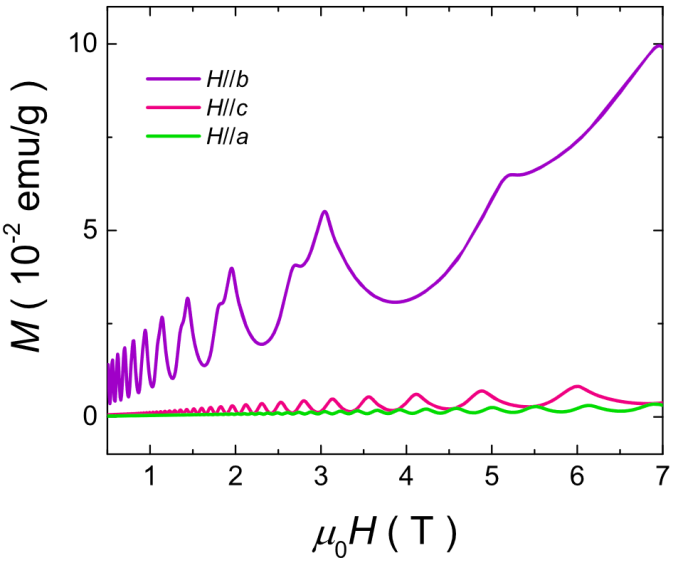

Supplementary Figure 6. Simulated magnetization curves for different magnetic field directions. The Fermi level is set to 31.85 meV (x = 0).

Supplementary Note 8: Diamagnetism-dominant magnetization

Supplementary Figure 7 shows each component of magnetization curves separately. With increasing temperature, the Berry paramagnetism decreases and eventually vanishes when E_F reaches the Dirac point at T_m, while the Berry diamagnetism starts to decrease at T_m. Note that the magnitude of the paramagnetic signal is smaller than that of the diamagnetic signal, resulting in that the total magnetization looks to be diamagnetic.

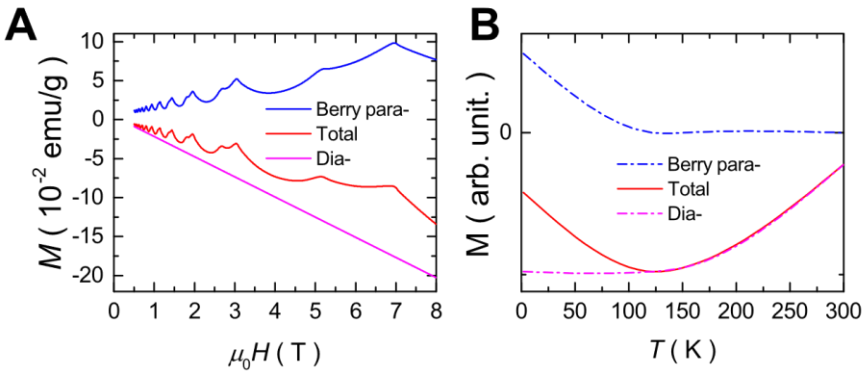

Supplementary Figure 7. Simulated field-dependent and schematic temperature-dependent magnetization. (A) Simulated field-dependent magnetization (red), which is the sum of the Berry paramagnetism of the conduction band electrons (blue) and diamagnetism of the valence band electrons (magenta). The diamagnetic component was obtained by fitting the experimental magnetization data. (B) Schematic plot of temperature-dependent magnetization (red).

SUPPLEMENTARY REFERENCES

1. Nair, N. L. *et al.* Thermodynamic signature of Dirac electrons across a possible topological transition in $ZrTe_5$. *Phys. Rev. B* **97**, 041111 (2018).

2. Hu, J., Xu, S.-Y., Ni, N. & Mao, Z. Transport of Topological Semimetals. *Annu. Rev. Mater. Res.* **49**, 207–252 (2019).

3. Wang, Z. *et al.* Highly mobile carriers in a candidate of quasi-two-dimensional topological semimetal $AuTe_2Br$. *APL Materials* **7**, 101110 (2019).

4. Moll, P. J. W. *et al.* Magnetic torque anomaly in the quantum limit of Weyl semimetals. *Nat Commun* **7**, 12492 (2016).

5. Zhang, C.-L. *et al.* Non-saturating quantum magnetization in Weyl semimetal TaAs. *Nat. Commun.* **10**, 1028 (2019).